Nature Communications

https://doi.org/10.1038/s41467-025-67845-8

Article in Press

Shock compression of FeOOH and implications for iron-water interactions in super-earth magma oceans

Received: 28 June 2025

Accepted: 10 December 2025

Cite this article as: Zhang, Y., Bali, K., Dorn, C. *et al.* Shock compression of FeOOH and implications for iron-water interactions in super-earth magma oceans. *Nat Commun* (2025). https://doi.org/10.1038/s41467-025-67845-8

Yanyao Zhang, Komal Bali, Caroline Dorn, Alessandra Ravasio, Hong Yang, Silvia Pandolfi, Amanda J. Chen, Xuehui Wei, Lélia Libon, Qijun Che, Donghao Zheng, Eglantine Boulard, Alessandra Benuzzi-Mounaix, Hae Ja Lee, Eric Galtier, Nicholas A. Czapla, Dimosthenis Sokaras, Roberto Alonso-Mori, Arianna E. Gleason, Sang Heon Shim, Guillaume Morard & Wendy L. Mao

Nature Communications format:

Shock Compression of FeOOH and Implications for Iron-Water Interactions in Super-Earth Magma Oceans

Yanyao Zhang[1]✉, Komal Bali[2]*, Caroline Dorn[2]*✉, Alessandra Ravasio[3]*, Hong Yang[1]*, Silvia Pandolfi[4]*, Amanda J. Chen[1]*, Xuehui Wei[5]*, Lélia Libon[4,6]*, Qijun Che[7], Donghao Zheng[8], Eglantine Boulard[4], Alessandra Benuzzi-Mounaix[3], Hae Ja Lee[7], Eric Galtier[7], Nicholas A Czapla[7], Dimosthenis Sokaras[7], Roberto Alonso-Mori[7], Arianna E. Gleason[1,7], Sang Heon Shim[5], Guillaume Morard[4,6], Wendy L. Mao[1,7]✉

[1]Earth and Planetary Sciences, Stanford University, Stanford, CA, USA.

[2]Institute for Particle Physics and Astrophysics, ETH Zürich, Otto-Stern-Weg 5, 8093 Zürich, Switzerland.

[3]Laboratoire LULI, CNRS - École Polytechnique - CEA - Sorbonne Université, F-91128, Palaiseau Cedex, France.

[4]Sorbonne Université, Muséum National d'Histoire Naturelle, UMR CNRS 7590, Institut de Minéralogie, de Physique des Matériaux et de Cosmochimie, Paris, France.

[5]School of Earth and Space Exploration, Arizona State University, Tempe, USA.

[6]ISTerre, Université Grenoble Alpes, CNRS, Grenoble, France.

[7]SLAC National Accelerator Laboratory, Menlo Park, CA, USA.

[8]Department of Geosciences, Princeton University, Princeton, NJ 08544, USA.

*These authors contributed equally to the work

✉e-mail: Y.Z (yanyaozh@stanford.edu), C.D. (dornc@phys.ethz.ch), R.A-M. (robertoa@slac.stanford.edu), A.E.G. (ariannag@stanford.edu), S.H.S. (shdshim@asu.edu), G.M. (guillaume.morard@cnrs.fr), W.L.M (wmao@stanford.edu)

Abstract (<= 200 words)

Iron(Fe)-water reactions in a magma ocean can influence water storage and density of planets. These reactions can form Fe-O-H phases, whose density, melting, and electronic properties at planetary interior conditions are important for informing planetary models. Here, we study natural goethite (α-FeOOH) that is shock-compressed along its principal Hugoniot. Analysis of our velocity interferometer system for any reflector (VISAR) results extends the equation of state

to over 800 GPa. X-ray diffraction and VISAR reflectivity results indicate the onset of melting occurs at ~95 GPa with complete melting by 166 GPa, which may be relevant to low seismic velocity anomalies observed above the core-mantle boundary. Analysis of X-ray emission spectroscopy results up to 285 GPa shows the spin crossover of Fe, with dominantly low spin Fe above ~265 GPa in the melt, supporting formation of dense basal magma oceans in terrestrial planets. Using our measured FeOOH densities, we model planetary interiors up to 10 Earth masses. Assuming FeOOH forms via iron-water reactions, the radius decreases by up to 28%, while the density increases by up to 165% compared to the unreacted cases, providing an avenue to investigate water storage and evolution in super-Earths and sub-Neptunes.

Keywords: FeOOH, laser shock compression, X-ray emission spectroscopy, X-ray diffraction, spin transition, melting, magma ocean, super-Earth, mass-radius relation

Introduction

The fate of water in super-Earths is critical to understanding their potential habitability. If present in sufficient amount, water in the interiors of super-Earths can also affect their interior structures and mass-radius relationship[1]. While some sub-Neptunes may accrete tens of percents of water by mass[2], most super-Earths have lower water mass fractions. The majority of super-Earths with well-characterized masses and radii are inferred to have less than 3% of water by mass[3], especially with Earth-like core mass fractions. Models that combined formation and evolution predict the population of super-Earths to be relatively dry[4,5]. However, these models considering thermodynamics suggest that water could be common (~1 wt%) in super-Earths[6]. For example, redox reactions could produce water endogenically from the oxidation of primordial hydrogen by reducing oxidized magma[7]. Hence, water is likely a common although limited component of super-Earths that formed during the lifetime of the proto-planetary disk. The majority of observed super-Earths are warm and hot worlds, allowing for the presence of magma-oceans even after Gyrs of evolution[1,8,9].

The distribution of water within super-Earth interiors influences not only their observed densities but also the evolution of their thermal profile, redox state, and atmospheric composition[10,11]. Therefore, determining how water is distributed between different depths, and how it chemically interacts with other compounds is essential for interpreting planetary data. These include both their mass-radius data from missions like Kepler, Transiting Exoplanet Survey Satellite (TESS), CHaracterising ExOPlanet Satellite (CHEOPS), and PLAnetary Transits and Oscillations of stars (PLATO) with radial velocity or transit-timing-variation-follow-ups as well as spectral data from missions like James Webb Space Telescope (JWST),

Extremely Large Telescope (ELT), or proposed Habitable Worlds Observatory (HWO) and Large Interferometer For Exoplanets (LIFE) mission.

Conventional super-Earth interior models assume a distinct water layer atop the rocky mantle[12]. When water partitions into the mantle or metallic core, it can reduce planetary radii at a given mass[13]. Additionally, the presence of water and the oxidation of iron are closely associated in magma oceans, with implications on the metallic core size and mantle composition[14]. Given the diverse fates of initial water inventories, it is crucial to investigate how iron and water together affect magma oceans under extreme pressure conditions. Previous high-pressure experiments have shown that metallic iron reacts with water to form FeO and FeH_x[15–17]. This scenario typically occurs in water undersaturated conditions in the present-day Earth's mantle. In water-rich environments, iron can be further oxidized and hydrogenated to form FeOOH phases[18,19]. The influence of these reactions on water storage and bulk densities of planets depends on the physical properties of iron hydroxide phases, which remain poorly understood under super-Earth interior conditions.

FeOOH crystallizes in an orthorhombic structure named goethite (α-FeOOH) under ambient conditions. It transforms into ε-FeOOH at ~6 GPa[20], and then dehydrogenates to form the pyrite-type FeO_2H_x (x = 0-1) at approximately 74 GPa and 1600 K[21]. The melting conditions of FeOOH are key information for the planetary interior model but have only been estimated by first-principles calculations[22]. Additionally, the predicted equation of state of liquid FeOOH is only available up to 140 GPa and 3000–6000 K[22], which is insufficient for modeling the interior structure of super-Earths with interior pressures of 0.5–1 TPa. Reaching such extreme pressures is a challenge with current static compression techniques, such as laser-heated diamond-anvil cells; and the long duration of laser heating can locally alter the system's stoichiometry due to fast hydrogen diffusion[23]. Shock wave compression presents a promising alternative, because it can not only achieve pressure-temperature conditions relevant to super-Earth interiors, but also likely preserve hydrogen in the sample due to the fast dynamic loading[24]. However, recent gas gun experiments on FeOOH have been limited to the solid-phase region (below 90 GPa and 2000 K)[25], leaving the melting pressure and the densities of liquid FeOOH unknown.

Another important property in constraining the magma ocean behavior is the iron spin state, which has been proposed to affect the iron partitioning between crystallizing solid and residual liquid[26,27]. Low-spin iron preferentially partitions into the melt at high pressures, potentially leading to the melt being denser than the coexisting solid and affecting magma ocean dynamics[26,27]. A high to low spin transition can itself reduce the volume of the host phase, resulting in a density increase. Iron in FeOOH undergoes the spin transition at ~50 GPa at 300 K based on previous X-ray emission spectroscopy (XES) and Mössbauer spectroscopy data in diamond anvil cells[28,29] and previous theoretical calculations[30,31]. This spin transition is accompanied by a ~10.9 % increase in density[29]. However, the spin state of liquid FeOOH under

high-pressure and high-temperature magma ocean conditions is currently unknown, leaving a critical gap in our understanding of silicate/oxide melts containing iron and water, and consequently their influence on planetary differentiation.

In this study, we performed laser shock compression experiments on natural goethite starting materials. Velocity interferometer system for any reflector (VISAR) measurements at the facility at Laboratoire pour l'utilisation des lasers intenses (LULI) allow us to determine the equation of state on the Hugoniot to over 800 GPa. In-situ X-ray diffraction (XRD) and XES measurements at the Matter in Extreme Conditions (MEC) end-station of the Linear Coherent Linac Source (LCLS) at SLAC National Accelerator Laboratory revealed the melting pressure (~95 GPa) and a spin transition in iron along the Hugoniot. Density data were incorporated into an interior model where iron reacts with water to form FeOOH, providing an avenue for understanding water storage and formation histories of super-Earths that formed under water-poor versus water-rich conditions.

Results and Discussion

Hugoniot Equation of State

The starting sample is natural goethite with the purity of 99.2 wt% (0.8 wt% SiO_2 + Al_2O_3 impurities) and the bulk density, ρ_0 = 4.236(81) g/cm^3 (see Methods for details; Text S1, Fig. S1, Table S1). The LULI experiments were conducted up to over 800 GPa, while the MEC experiments were conducted below 100 GPa. Step targets were used for both experiments, impedance match methods were used for data analysis, and Monte Carlo simulations were used to evaluate uncertainties. Details of target design, experiments, and data analysis can be found in the Methods and the supporting information (Texts S2, S3; Figs. S2-S4).

Combined LULI and MEC data show that U_S increases linearly as U_P increases (Fig. 1; Table S2). A linear fit to all data yields U_S = 3.9(3) + 1.6(1)U_P. Our data at U_P < 3 km/s is consistent with previous gas gun data which show a plateau at U_P = ~2 km/s[25] (inset in Fig. 1c). However, we are unable to discriminate between a potential plateau and a linear trend, particularly at U_P < 2 km/s; the resulting fit shows negligible variation whether the full dataset is used or restricted to U_P > 2 km/s (Fig. S5). Using this relation, pressure was calculated using the equation of $P = P_0 + \rho_0 U_P U_S$, where P_0 is the ambient pressure (Table S2). We reached the maximum pressure of 819(72) GPa in our experiments, which is relevant to the interior pressure of super-Earths.

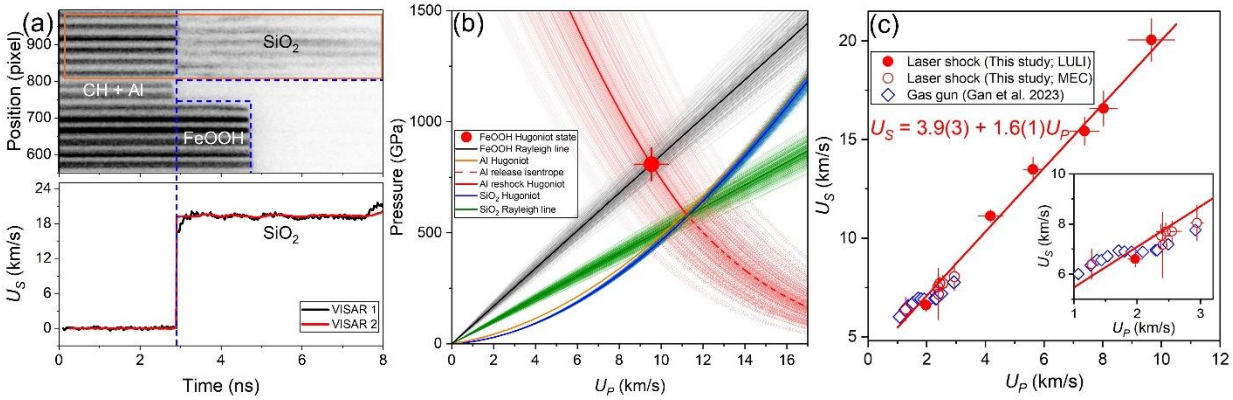

Figure 1. VISAR analysis and results. (a) A representative VISAR image at 819(72) GPa from LULI experiments and its corresponding shock velocity (U_S) versus time at the SiO_2 window side. The orange rectangle shows the fringes used in the analysis. (b) The U_S of SiO_2 was used in an impedance matching method with Monte Carlo simulations to derive the Hugoniot state of Al first and then of the FeOOH sample in the pressure-particle velocity (P-U_P) space. (c) Shock velocity (U_S) versus particle velocity (U_P) for FeOOH. Red circles with error bars are U_S-U_P data from this study, while open blue squares with error bars are from a previous gas gun study[25]. A linear function was used to fit our LULI and MEC data (red line). Insert is a zoom-in showing U_P below 3.2 km/s.

To evaluate potential hydrogen preservation during shock compression, we consider the rise time of the drive laser power, $t = 10^{-10}$ s, in our laser shock experiments. The hydrogen diffusion coefficient, D_H, is unknown in the liquid FeOOH under our experimental conditions. Instead, we used D_H of 10^{-3} cm^2/s in superionic liquid water at 400-600 GPa and ~5000 K as an upper bound approximation, where hydrogen is unbounded to any other atoms and moves freely across the entire sample[23]. The diffusion length is thus at most $L = \sqrt{D_H t} = 10^{-6.5}$ cm. Our sample is 10^{-1} to 10^{0} cm in length and width and 4 to 5×10^{-3} cm in thickness. Therefore, even if superionic behavior is taken into account[32], hydrogen is likely to stay in the atomic structure of the sample during the laser shock. Furthermore, the full width at half maximum of the X-ray beam is 3×10^{-3} cm in diameter. Thus, hydrogen is likely to stay within the XRD probing area, although it is difficult to completely rule out the possibility of hydrogen loss because D_H in our sample at the relevant pressure-temperature conditions is not well constrained.

Melting pressure and temperature

In-situ XRD patterns and VISAR reflectivity measurements were used to evaluate the melting pressure of FeOOH along the Hugoniot. Two criteria were applied to identify melting. The first

is the emergence of diffuse scattering, which may coexist with diffraction peaks, and is indicative of the onset of melting[33]. The second criterion involves a change in reflectivity at the rear surface of the window, commonly associated with the solid-to-liquid transition of the ejected material[34].

To focus on detection of diffuse scattering, which is much weaker than crystalline diffraction peaks, we masked diffraction peaks from solid phases (Figs. 2a and 2b). At 1 atm, masked diffraction patterns show relatively flat intensity above 15°, compatible with background (Fig. 2b). The signal below 15° results from kapton[35]. At 95 GPa, the masked pattern starts to show two broad scattering features at 16° and 22° 2θ angles, indicating that a small amount of melt is beginning to form while the shocked FeOOH is still predominantly solid (Fig. 2b). The intensity of the diffuse scattering increases as pressure increases to 138 GPa where the diffraction spots are still observed (Fig. 2b). This observation indicates coexistence of the solid and melt at this pressure. Dehydration has been reported in previous diamond-anvil cell experiments[21,36,37], but not observed here. Laser shock compression has a compression rate in the order of 10^{12} GPa. Such ultrafast compression may lead to solid-melt coexistence and suppress dehydration due to kinetic limitations. At 166 GPa, crystalline diffraction peaks were no longer observed, and only diffuse scattering is present (Fig. 2b), indicating the melting completes by 166 GPa (Fig. 2c).

The loss of fringe motion at the sample-vacuum interface serves as additional evidence of melting, likely resulting from the loss of strength upon melting of FeOOH, as suggested by previous studies on shock-compressed SiO_2[34]. The VISAR images at 95 GPa (Fig. S6) show a gradual disappearance of fringe motion from the edge to the center. Since the drive laser is focused at the image center, the laser power decreases from the center to the edge. Hence, this change in fringe motion is indicative of onset melting at the center which is consistent with our XRD data (Figs. 2a and b). This onset pressure is slightly lower than that predicted from previous first-principles calculations[22,38] (Fig. 2c). At 138 GPa, the fringe motion vanishes in the whole VISAR images (Fig. S6), indicating that the sample is within the melting region.

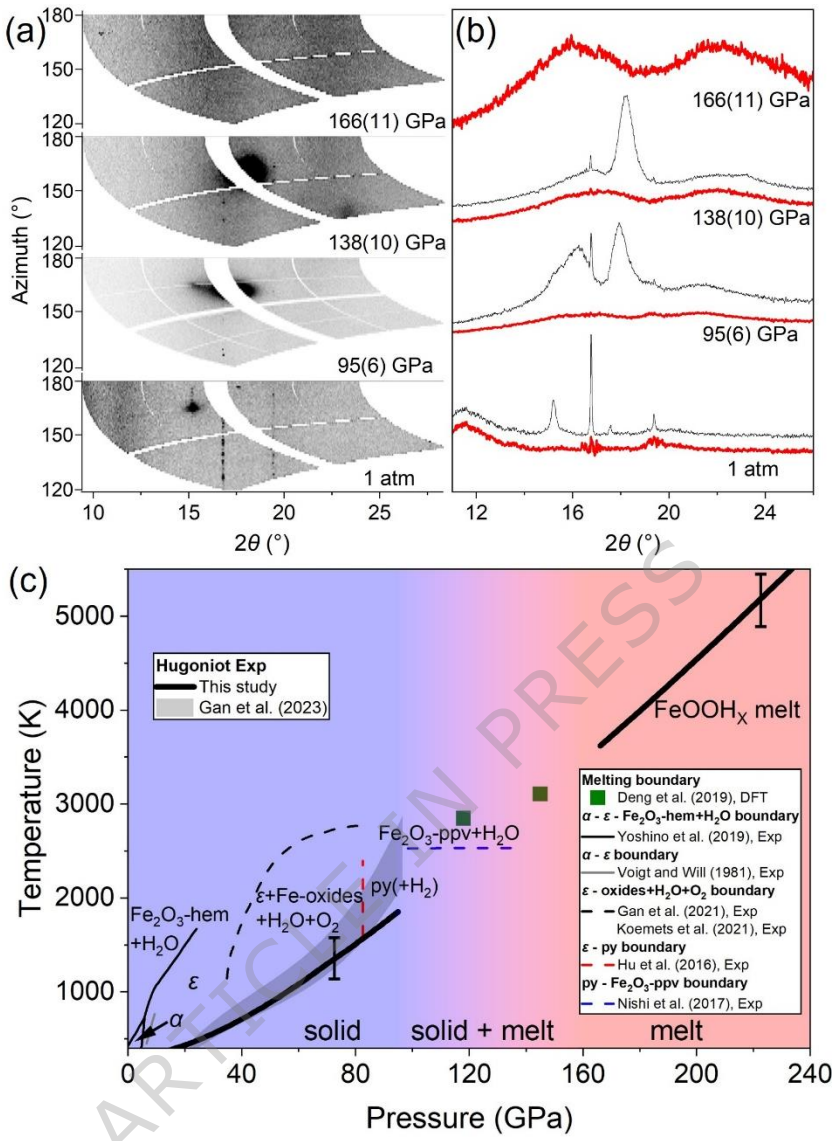

Figure 2. FeOOH melting along the Hugoniot. (a) XRD images at 1 atm and high pressures (wavelength of 0.6818 Å). Their corresponding integrated patterns are shown by the black lines in (b). The red lines show diffuse scattering features when the diffraction spots are masks. (c) Hugoniot temperature-pressure path of FeOOH. Our calculated Hugoniot curve (thick black lines with error bars) is plotted on top of the phase diagram of FeOOH[21,22,36,39–42]. Exp, experiment; DFT, density functional theory; *α*, goethite; *ε*, $CaCl_2$-type FeOOH; hem, hematite; ppv, post-perovskite phase. The blue, purple, and red areas show pressure regions for solid, solid + melt mixture, and melt, respectively, along the Hugoniot.

The temperature along the Hugoniot can be estimated using the equation of $dT = -T\left(\frac{\gamma}{V}\right)dV + \frac{(V_0-V)dP+(P-P_0)dV}{2C_V}$, where γ is the Grüneisen parameter and C_V is the heat capacity

at a constant volume[43]. γ is assumed to have a form of $\gamma = \gamma_0 \left(\frac{\rho_0}{\rho}\right)^q$, where the subscripted '0' denotes the ambient conditions and q is a volume-independent constant. C_V can be calculated using the Debye model[43] with Debye temperature at ambient conditions, θ_0. The γ_0, q, and θ_0 of goethite were taken from Gleason et al.[20] as 0.91, 1, and 740 K, respectively. As temperature approaches to the melting point, the electronic and anharmonic effect on γ and C_V may be significant, but experimental constraints are not available. For this reason, in the pressure range of 70-95 GPa we used parameters from theoretical calculations[22], specifically C_V of 130 J/mol/K and γ of 1.84 for pyrite-type FeO_2H. Our calculated temperature for solid FeOOH increases from 300 K to approximately 1855 K at 95 GPa (Fig. 2c), consistent with a previous gas gun study[25]. Furthermore, previous theoretical calculations suggest that C_V remains nearly constant at 139.6 J/mol/K while γ increases with increasing pressure (γ_0 = 0.876 and q = -0.914) in liquid FeOOH. Our calculated temperature for liquid FeOOH increases from approximately 3620 K at 166 GPa to approximately 7543 K at 300 GPa (Fig. 2c).

Previous static compression experiments in diamond-anvil cells have suggested that the pyrite-type FeO_2Hx phase could account for the anomalously low seismic velocities observed in ultralow-velocity zones above the core-mantle boundary[18]. Our study reveals that the melt and solid phases may coexist at the core-mantle boundary. The presence of the melt would further enhance the velocity decrease so less FeOOH phase is needed to explain ultralow-velocity zones.

Electronic spin transition

Electronic properties along the Hugoniot were investigated by in-situ XES measurements using an XFEL. Our emission spectra at ambient conditions consist of the main peak $K\beta_{1,3}$ and the satellite peak Kβ' (Fig. 3a), consistent with previous FeOOH data in the high spin state[29]. At high pressures along the Hugoniot, the main peak shifts to a lower energy and the intensity of satellite peak reduces, indicating that a fraction of the iron in the shock-compressed FeOOH transforms to a low-spin state (Figs. 3a and S7). We calculated the integrated absolute difference (IAD) between reference and shot spectra[44]. As the low spin spectrum remains unknown, we used the high spin emission spectrum at ambient conditions as a reference. Our emission measurements have high accuracy due to experimental geometry, X-ray energy, and probing time (see methods). The precision was evaluated similar to the method in Pardo et al.[45] The noise oscillation of our spectra is approximately 3% relative to the height of the main peak. Using a Monte Carlos method, we generated 1000 emission spectra with 3% random variation to each data point, and calculated IAD for each spectrum. The obtained 1000 IAD values display a normal distribution from which the mean value and the standard deviation were obtained (Fig. S8; Table S3). The obtained IAD values and their uncertainties are plotted in Fig. 3b. The

applied 3% variation in the emission spectra results in only 3-5% uncertainties in the IAD values, indicating robustness of using IAD values to indicate spin state.

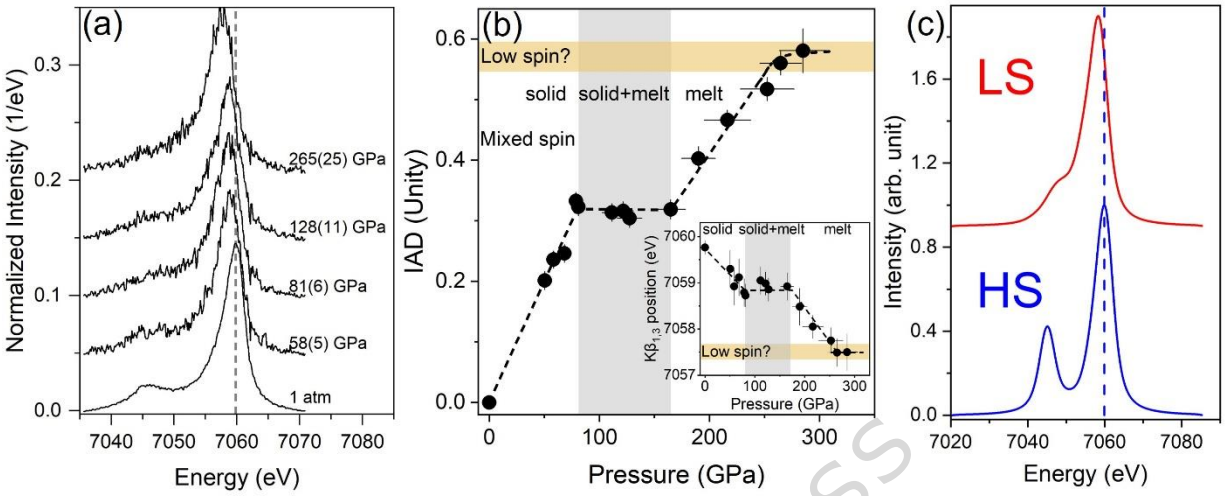

Figure 3. Electronic spin transition in FeOOH. (a) Representative XES spectra at 1 atm and high pressures. The spectra are vertically offset for better visualization. The vertical gray dashed line marks the main peak position at 1 atm, relative to which the main peak shifts to lower energy at high pressures. (b) Integrated absolute difference (IAD) with error bars versus pressure. Inset shows the position of the main $K\beta_{1,3}$ peak with error bars as a function of pressure. Dashed lines are drawn to indicate data trends. The yellow horizontal bands indicate the IAD value likely consistent with dominantly low-spin Fe. The gray vertical bands show the pressure region of coexisted solid and melt along the Hugoniot (Fig. 2c). (c) Simulated Fe^{3+} Kβ XES spectra with high-spin (HS, 10 *Dq* = 1.8 eV) and low-spin (LS, 10 *Dq* = 3.6 eV) states. The vertical dashed line denotes the main peak position of the HS spectrum.

The IAD increases from zero at ambient conditions to ~0.3 at 81 GPa. The emission spectrum at 81 GPa shows the weak satellite peak Kβ' (Fig. 3), indicating that the fully low spin state has not been reached, i.e., mixed spin state. This observation is different from a previous study in diamond anvil cells which shows the low spin Fe in goethite above 45 GPa at ambient temperature[29]. The difference indicates that the high temperature in our shock experiments broadens the spin transition region, as observed in other materials such as magnesiowüstite[46].

The IAD values and the main peak position do not change much between 81 to 165 GPa. At this pressure region, melting was identified as discussed above (Fig. 2). As such, the measured emission spectra in this pressure range contain information from both solid and liquid phases. By extending the IAD trend of the solid phase (below 81 GPa) to higher pressures and the liquid phase (above 165 GPa) to lower pressures, we find that the plateau region could be caused by a mixture of signals from the low-spin-dominated solid and the high-spin-dominated liquid phases.

That is, the melting may lead to the spin "recovery" from low to high. The loss of structural order upon melting weakens Fe-O interactions which reduces covalency, leading to a diminished crystal field splitting as a consequent "recovery" of the high-spin state.

At pressures above 165 GPa, the IAD increases and the main peak position shifts to lower energies, indicating that the low-spin fraction increases with increasing pressures in the melt (Fig. 3a). Evidence that the iron in the melt may reach the fully low spin state above 265 GPa include 1) the emission spectra showing no observable satellite peak Kβ', 2) the IAD reaching to 0.5-0.6 that has been linked to low-spin iron in iron compounds[47], and 3) the IAD and main peak positions remaining unchanged within experimental uncertainties for the highest pressures (Fig. 3b). We also simulated Fe^{3+} Kβ XES spectra using the crystal field multiplet theory[48,49] in the CTM4XAS program[50]. The spin transition from the high-spin to low-spin state occurs at a crystal field splitting energy of about 3.0 eV. We used 10 Dq = 1.8 eV for the HS state and 10 Dq = 3.6 eV for the LS state. The theoretical Fe^{3+} XES show well agreement with the experimental observations. Upon the high-spin to low-spin transition, the main $K\beta_{1,3}$ line exhibits a negative energy shift, while the Kβ' feature shifts to higher energy (Fig. 3c). The reduced Kβ'-$K\beta_{1,3}$ splitting reflects an increase of covalency, associated with the increase of crystal field. In addition, the ratio of Kβ'/$K\beta_{1,3}$ reflects S/(S + 1). All these changes originate from the strong 3p-3d exchange interaction, which plays a dominant role in the Kβ emission channel.

These results indicate that iron- and hydrogen-rich melts, which are likely to form during the late stages of fractional crystallization, can exhibit varying proportions of low-spin iron depending on depth and the size of the super-Earth[51]. In larger super-Earths with deeper magma oceans, a greater proportion of low-spin iron may be stabilized. If low-spin iron preferentially partitions into the melt[26,27], it could become denser than the coexisting solid, potentially leading to the formation of a basal magma ocean in a super-Earth interior.

Density of FeOOH along the Hugoniot

Densities along the Hugoniot can be calculated using the equation of $\rho = \rho_0/(1 - U_P/U_S)$ (Fig. S9; Table S2)[43]. This equation is derived from the mass conservation which is universal regardless of phase transitions. Thus, we used ρ_0 of our starting sample for all different phases/structures along the Hugoniot. The density increases significantly from 4.236 g/cm^3 at ambient conditions to approximately 6.8 g/cm^3 at 196 GPa, and then slowly increases to approximately 8.3 g/cm^3 at 819 GPa (Fig. S9). The different slope is due to the pressure effect on compressibility and/or different solid versus liquid compressibility. Using the EOSfit7 software[52], we fit the P-ρ data of FeOOH melt data at pressure above 166 GPa to the second-order Birch-Murnaghan EOS. We used a reference pressure of 196 GPa where the density is 6.8(4) g/cm^3 from our LULI data (Table S2). The bulk modulus at this reference pressure was

obtained to be 1407(423) GPa. The density information is further used in the planetary interior model in the next section.

Planetary interior model

We investigate the implications of the formation of FeOOH on interior models of planets. Specifically, we are interested in the effect on planet bulk density, which we will quantify in the following, and on the potential gas speciation from outgassing, which we address speculatively in the discussion.

For investigating the effect on planet bulk density, we employ the interior model from Dorn et al.[53] with recent updates in Luo et al.[13] (refer to Methods for details). For the choice of the interior model, we are guided by the chemical reactions based on previous mineral physics experiments[15,16,18,19]:

$$3Fe + H_2O \rightarrow FeO + 2FeH \ (P < 86\ GPa) \quad (1)$$

$$4Fe + 2H_2O \rightarrow FeOOH + 3FeH \ (P > 86\ GPa) \quad (2)$$

Reaction (1) involves two processes: first, Fe is oxidized by H_2O to form FeO and H_2; then, the generated H_2 further reacts with additional Fe to form FeH[54]. We seek to explore what the effect of this reaction is on the bulk density of planets. Our reference case (case A) is according to commonly used interior models in exoplanetary science that assume pure iron cores and iron-free silicate mantles with water only added to the surface (case A in Fig. 4, and green curves in Fig. 5a). The largest effect of reactions (1) and (2) can be studied focusing on a hypothetical end-member case (case C in Fig. 4), where all the iron in the mantle takes part in reaction (1) and (2) depending on the pressure range. If all the iron is reacting with water assuming an Earth-like interior (i.e., a core mass fraction f_{core} of 0.325), the amount of water is constrained to values below 5 wt%, depending on the planet mass. The upper limit of 1.3 wt% can be understood from considering only reaction (2) and is derived from the molar ratio of reactants and the molar mass ratios of water (M_{H2O}) and iron (M_{Fe}). Specifically, since only one out of four Fe atoms is oxidized to FeOOH in reaction (2), we assume that 25% of the total Fe participates in the reaction. Accordingly, the water mass fraction f_{H2O} equals to $0.25*f_{core}*(M_{H2O}/M_{Fe})*(2/4)$, where M_{H2O} and M_{Fe} are equal to 18.015 and 55.845 g/mol, respectively. When we allow for the formation of FeO and FeOOH (case C), we keep the same bulk composition as in case A, but all water is now chemically bound to FeO and FeOOH in the mantle[15–17] and FeH in the core. At higher planet masses, the pressure gradient in the interior is steeper and hence the mass fraction of the planet experiencing pressures above 86 GPa, where FeOOH is stable, becomes larger. The formation of 1 mole FeOOH requires 1 mole more water more than the formation of 1 mole FeO. In consequence, the amount of water required to fully react iron is 1.3 wt% for a 1 $M_\oplus$ (Earth mass) planet. Here, we depict the molten silicate mantle with a 2-layer structure, according to the

stability regions of FeO and FeOOH. As convection of magma oceans is very vigorous, a layered structure is unlikely to establish[1,8,9]. Here, we simply represent the mantle to be a mixture of silicates with FeO and FeOOH, depending on pressure. The actual distribution of FeO and FeOOH in combination with a vigorously convecting magma ocean model is outside the scope of this study.

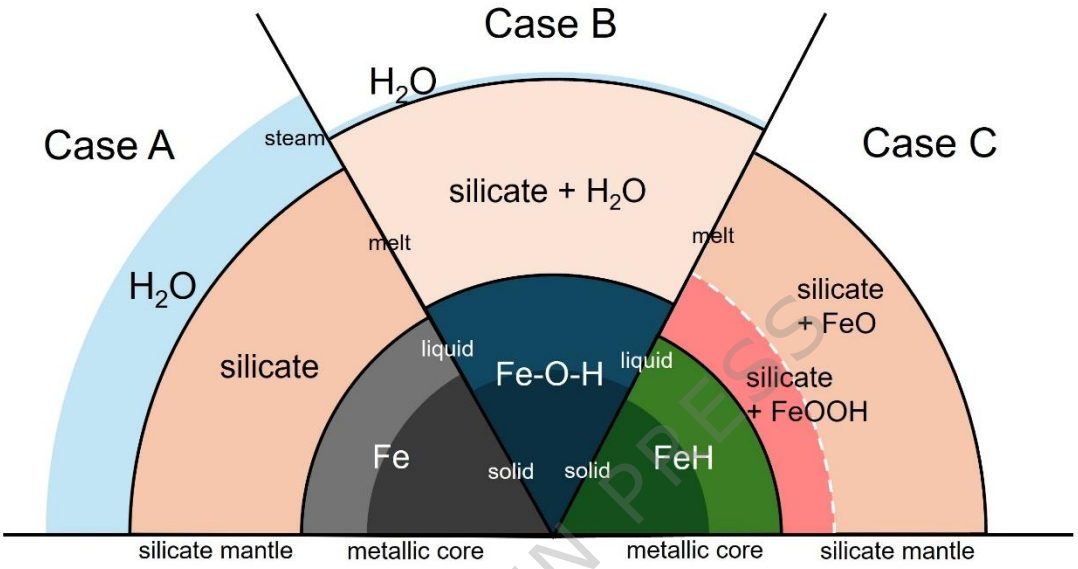

Figure 4. Schematic of investigated interiors of magma ocean worlds. Case A is the reference case of an iron-free silicate mantle, a pure iron core, and a water steam envelope on top. Case B has the same bulk composition as case A. Case B allows for the water to be dissolved in mantle melt and in the core[13]. Case C includes the formation of FeOOH and FeH by the reaction of water and iron. White dashed line in case C denotes 86 GPa. The formation of FeOOH is considered for pressures above 86 GPa while the formation of FeO is considered for pressures below 86 GPa, although a strictly layered structure may not exist (see the main text).

The main effect of accounting for reactions (1) and (2) in case C compared to commonly used interior models (case A) is a reduction by ~6-28% in radii which implies a density increase of ~22-165% (Fig. 5a). Compared to case A, the core in case C shrinks by about 1/3-1/4 and the mantle expands as O and H are added to the mantle (Fig. 4). This combined effect causes the radius at the top of the mantle in case C to increase marginally (1.5-3%). Thus, the total radii reduction in case C is dominated by the lack of any steam water layer at the surface as water stores in the interior of the planets following reactions (1) and (2).

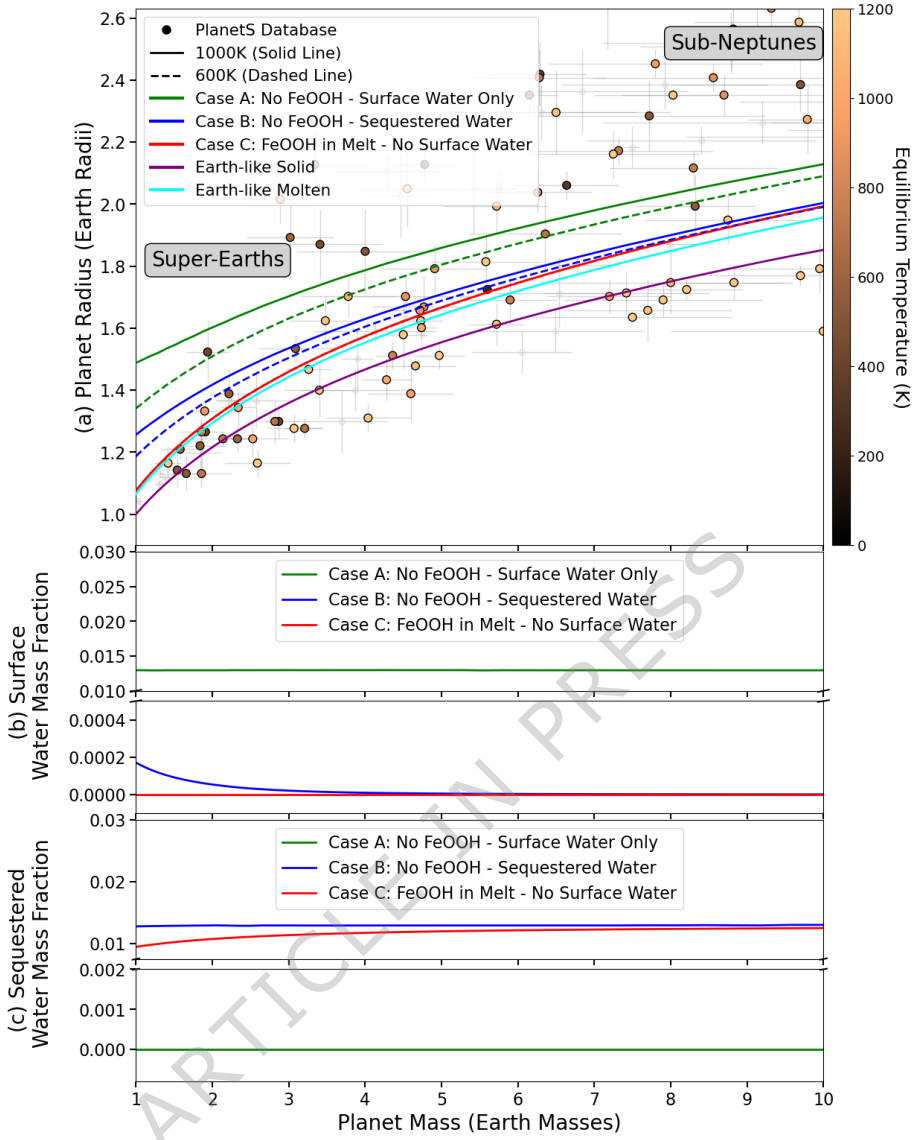

Figure 5. Results of our interior model with consideration of iron and water reaction to form FeOOH. (a) Mass-radius relationships of investigated interior scenarios (lines) plotted against well-characterized exoplanets from the PlanetS Database[55] (circles with error bars). As black-body temperatures vary widely for the observed population, we use 600 K (dashed lines) and 1000 K (solid lines) for the interior models. (b) Mass fraction of surface water for cases A, B, and C. (c) Mass fraction of sequestered water for all cases.

Also, our hypothetical end-member case C yields smaller radii compared to case B when water is allowed to be dissolved as O and H in the (core and mantle) melts according to solubilities and partitioning coefficients as done in Luo et al. 2024[13] (Fig. 5). This is expected as

case B includes a steam water layer by definition, which significantly increases planet radii compared to bare rocky worlds.

Our mass-radius curves span a region from super-Earths to sub-Neptunes. Here, we now focus on the end-member scenario where we allow for the maximum amount of water that is needed to react all iron according to reactions (1) and (2), which varies from 0.9-1.3% across the planet mass range of interest. Interestingly, this value is lower than the 3% of water that has been inferred to be an upper bound on the possible amount of water for the majority of super-Earths[3] given observational data. In addition, most observed super-Earths are hot worlds that likely underwent significant atmospheric loss due to their proximity to the host star[56]. This implies that the amount of water available for chemical reactions early in the history of the planet may not be present at the time of observation. With case C we highlight a case when no water is present at the surface; however, not all available water may have reacted with iron early in a planet's history and some water can be dissolved in silicates or remain present at the surface. Our hypothetical end-member scenario highlights that the treatment of water in interior models has profound implications for the interpretation of observational results. Treating interactions between water and iron (case C, red) leads to radii that are matched in the super-Earth population, however, the identical bulk composition with a commonly layered model (case A, green) leads to a mass-radius curve that lies in a transitional regime between super-Earths and sub-Neptunes where only few planets are observed. However, we note that for realistic super-Earths, not all iron may have reacted with water as the reactants may be partially separated in growing super-Earths interiors and likely not all iron participates in reactions (1) and (2) or the amount of water is simply limited well below 3%. Furthermore, we do not consider any silicates to be part of the reaction system as the experiments are restricted to iron and water only. Therefore, case C is a hypothetical end-member case.

Where does the water come from? Although water can be added primordially when building blocks from outside the water snowline are accreted[57], water can also be formed endogenously by redox reactions between FeO and any primordial hydrogen envelope, which has been estimated to lead to water amounts in the range of 1%, so roughly similar to our end-member case C. If only 1 wt% of water is available, almost all of the available iron in Earth-like interiors can react to form FeOOH, ignoring any interaction of silicates. In principle, O and H can also partition to the metal phase during core formation, which we have not taken into account here. Chemical thermodynamic approaches are needed to take this consistently into account.

The exoplanet community is eager to learn which super-Earths evolved from the sub-Neptune population via atmospheric loss and which super-Earths were born rocky[58]. Differences in bulk composition and their effect on bulk densities are significant (Fig. 5). The chemical imprint of hydrogen envelopes or the lack thereof on the chemistry of super-Earth atmospheres is another

promising avenue for distinguishing the planetary evolution histories[6] thanks to missions like JWST, ELT, HWO, and LIFE.

The imprint of FeOOH formation on the gas speciation of any outgassing secondary atmosphere is therefore of broad interest. FeOOH-rich mantles likely outgas more oxidized species compared to mantles containing FeO. Clearly, the higher oxidation power of FeOOH compared to FeO provides the possibility to distinguish dry super-Earths from water-rich worlds.

Methods

Sample characterization and target design

Our starting samples are natural goethite from the Restormel Royal Iron Mine, Cornwall U.K. They exhibit an acicular or prismatic crystal habit and a size of a few millimeters in width and height and approximately a centimeter in length (Fig. S1). Single-crystal XRD analysis[59] reveals that the sample has orthorhombic symmetry (space group *Pnma*) with lattice parameters of a = 9.9506(6) Å, b = 3.0190(2) Å, c = 4.6001(3) Å, V = 138.191(15) Å^3, and ρ_0 = 4.2707(5) g/cm^3, consistent with the goethite structural parameters at ambient conditions (Text S1; Table S1)[60]. Density measurements using the Archimedes method give a density of 4.236(81) g/cm^3, based on the mean and standard deviation calculated from seven analyses. The consistent results for densities derived from XRD and the Archimedes method indicate negligible porosity within measurement uncertainties. Energy-dispersive X-ray spectroscopy (EDS) shows a homogeneous FeOOH composition with approximately 0.8 wt.% SiO_2 + Al_2O_3 impurities (Text S1; Fig. S1).

The samples were double-sided polished to a thickness of 35-45 µm using 3M diamond films, and the thickness was measured using a micrometer. To enhance the reflectivity in the VISAR measurements, a 300 nm thick Al coating was deposited on one side of each sample. Step target designs were used in both the LULI and MEC experiments. The LULI step target consists of a 10 or 50 µm thick kapton ablator, a 40 µm thick Al foil serving as a pusher to create a uniform shock wave, a 44-200 µm thick SiO_2 or LiF window material attached to one half of the Al surface, and the sample on the other half. A small gap of a few µm between the sample and the window allows for determining the breakout time of the kapton (Fig. S2a). In the MEC experiments, the Al-coated sample platelets were glued to one half of the Al-coated kapton surface, with the kapton having a ~80 µm thickness (Fig. S2b).

Laser-driven shock experiments

The experiments were performed at the LULI 2000 high-energy laser facility, utilizing two laser beams at a wavelength of 527 nm with either 2 ns or 5 ns square pulses. Each laser pulse has a

single-pulse energy of up to 500 J. Phase plate smoothing was employed to produce an 800 μm diameter focal spot, achieving a maximum intensity of 10^{14} W/cm^2 on the target when both laser beams were combined. Diagnostics such as VISAR were used to measure the reflectivity and shock velocity along the Hugoniot at wavelengths of 1064 nm (ω) and 532 nm (2ω).

Laser-driven shock compression experiments have been performed using the frequency-doubled Nd-glass laser beams available at the MEC end-station of LCLS at SLAC National Accelerator Laboratory. We produced Hugoniot states inside the sample by using flat-top temporal pulses of 8 ns with focal spots of 300 μm diameter on target using continuous phase plates available at MEC. The hydrodynamics was monitored using two velocity interferometry systems for any reflector (VISAR) operating at 532 nm.

VISAR data analysis

VISAR images in the LULI experiments show fringe motion in the LiF or SiO_2 window and the transit time of the shock wave inside the sample. Analysis of the fringe motion using the Neutrino software, together with the Hugoniot of LiF and SiO_2[62,63], reveals U_P in LiF or U_S in SiO_2. Note that the shock front in SiO_2 becomes reflective at pressures above approximately 100 GPa along the Hugoniot [61]. The transit time and sample thickness were used to calculate U_S in the sample. U_P and P of the sample can be further constrained using an impedance matching technique from the release isentrope and the reshock Hugoniot of Al[43] (Text S2). The mean and standard deviation of U_P and P were obtained by running 300 Monte Carlos simulations with consideration of uncertainties of Hugoniot parameters of the window and Al, the fringe motion analysis, the sample initial density, and the transit time in the sample (Text S2).

VISAR images from the MEC experiments provide the transit time of the shock wave inside the kapton. Using a previous Hugoniot of kapton and the Hugoniot of goethite FeOOH from our LULI experiments, the sample's U_P and P were constrained by employing an impedance matching method [43] (Text S3). Also, 1000 Monte Carlos simulations were performed to derive the frequency distribution of U_P and P in sample with uncertainty sources of the transit time in kapton and Hugoniot parameters of both kapton and goethite FeOOH. The mean and standard deviation of U_P and P were finally calculated from the frequency distribution.

XES and XRD

In-situ Kβ XES spectra or XRD patterns were collected during laser shock compression at LCLS, MEC, following the previous experimental setups[33,51]. X-ray pulses are approximately 50 fs wide and are quasi-monochromatic with only 0.2-0.5% energy variation. X-ray beam focuses down to 30 μm in diameter in the center of the uniformly shocked area on the sample. X-ray

probing time is 0.5-1 ns prior to the sample breakout so that both emission and diffraction probe uniformly shocked samples.

X-ray energy was set to 8 keV for XES measurements. We used a multi-crystal energy dispersive spectrometer where a crystal analyzer and a position-sensitive detector (PSD) follow the von Hamos geometry[64]. The analyzer was placed at the 90° angle horizontally to the incident X-ray to avoid elastic scattering. The analyzer consists of arrays of bent crystals. The curvature of these crystals is used to focus X-rays emitted from the sample onto the PSD. The direction perpendicular to this curvature is responsible for dispersing X-ray energies across the PSD. By integrating the PSD signal along the focusing at different energies, an emission spectrum is obtained. This geometry allows us to collect most of the mission signal from the first 10 μm of compressed sample[51].

X-ray energy was set to 17 keV for XRD measurements. The diffraction data were collected using four ePix10k detectors which were placed in the standard detector configuration at MEC, LULI[33]. We used LaB_6 to calibrate the tilting and the distance to the sample of four detectors in the Dioptas software[65]. Further data analysis was performed in the same software.

XES spectra simulation

We simulate the Fe^{3+} Kβ XES spectra using the crystal field multiplet theory[48,49] implemented in the CTM4XAS program[50]. Fluorescence emission was considered part of the x-ray inelastic scattering and can be described by the Kramers-Heisenberg equation[66]. Kβ XES mutiplets are fully considered, including 3d-3d, 1s-3d, 3p-3d interactions, 3d spin-orbit coupling (SOC), and crystal field splitting. The Slater integrals F^{dd} and F^{pd} were scaled to 80% of their Hartree-Fock values, while G^{pd} was scaled to 56%. Temperature effects use the Boltzmann weighting factor. The core-hole lifetime broadening and instrumental resolution were modeled using a Lorentzian function with a half-width at half-maximum (HWHM) of 1.5 eV and a Gaussian function with a HWHM of 1.2 eV, respectively. Due to the symmetry distortion in FeO(OH), a distorted D_{4h} symmetry was considered in the XES calculations, where *Ds* and *Dt* considered as 0.1 eV and 0 eV, respectively. These specific numerical values are not critical for this study. The simulated high-spin spectrum was energy-shifted to align with the experimental spectrum at 1 atm. The Fe^{3+} ion ($3d^5$) has a high-spin ground state corresponding to the $^6A_1$ term. In the low-spin configuration, the ground state becomes the $^2T_{2g}$ term. A crystal field splitting energy (10 *Dq*) of approximately 3.0 eV is required to induce the spin transition from the high-spin to the low-spin state.

Interior model

The interior model from Dorn et al.[53] with recent updates in Dorn & Lichtenberg[1] and Luo et al.[13] solves hydrostatic equilibrium, mass conservation, and equations of state. Here, we consider an iron dominated core, a silicate dominated mantle and a water (steam) layer. For the core, we consider Fe, H, and O, if allowed. For solid Fe, we use the equations of state for hexagonal close packed (hcp) iron from literature[67,68]. For liquid iron with, and without H and O, we use Luo et al.[13]. The core thermal profile is assumed to be adiabatic throughout the core. At the core-mantle boundary (CMB), there is a temperature jump as the core can be hotter than the mantle due to the residual heat released during core formation. We follow Stixrude et al.[69] and add a temperature jump at the CMB such that the temperature at the top of the core is at least as high as the melting temperature of the silicates.

The mantle is assumed to be made up of three major constituents, i.e., MgO, SiO_2, and FeO/FeOOH. For the solid mantle, we use the thermodynamical model Perple_X[70], to compute stable mineralogy and density for a given composition, pressure, and temperature, employing the database of Stixrude et al.[71]. For pressures higher than 125 GPa, we define stable minerals a priori and use their respective equation of states from various sources[72–76]. For the liquid mantle, which is the focus of this work, we calculate its density assuming an ideal mixture of main components (Mg_2SiO_4, SiO_2, and FeO)[73,77–79] and add them using the additive volume law. Note that we use Mg_2SiO_4 instead of MgO since the data for forsterite is available in a high-pressure temperature regime, which is not available for MgO to our knowledge. The temperature gradient is assumed to be adiabatic, and for multi-component mixtures, we use the harmonic mean of the single-component adiabatic gradients.

Water can be added to the mantle melts, while the solid mantle is assumed to be dry. The addition of water reduces the density, for which we follow Bajgain and coauthors [80] and decrease the melt density per wt% water by 0.036 g/cm^3. For small water mass fractions, this reduction is nearly independent of pressure and temperature.

The melting curve of mantle material is calculated for dry and pure $MgSiO_3$ to which the addition of water[81] and iron[82] can lower the melting temperatures. The presence of H and O within the core will also lower its melting temperature, for which we follow Luo et al.[13].

The partitioning between mantle melts and the water layer is determined by a modified Henry's law, for which we use the fitted solubility function of Dorn & Lichtenberg[1]. For the partitioning of water between iron and silicates, we follow Luo et al.[13]. For the equilibration pressure of water to partition between iron and silicates, we use half of the core-mantle boundary pressure, which is roughly within typically discussed values for Earth (0.3-0.6). Varying this pressure would introduce overall small changes in the distribution of water.

Above the mantle, a water layer can be present. For most scenarios that we investigate here, water at the surface is in steam phase. We employ the EOS compilation of different water phases

from Haldemann et al.[83]. We further assume an adiabatic temperature profile in the steam phase except for pressures below 0.1 bar, where we assume an isothermal profile following the equilibrium temperature. The radius of the planet is defined at 1 mbar. For our interior model, we use EOS for Fe[13,67,68] in the core instead of FeH. The effect of H on the density of FeH is minor because hydrogen atoms are much smaller than iron atoms, and thus the volume change from Fe to FeH is minimal. The effect of using Fe versus FeH in the core on the radius is less than ~0.5%, which we quantify by density differences between the employed Fe EOS and the FeH EOS[84].

Data Availability

The experimental results are provided in tables in the Supplementary Information. The raw data can be provided upon reasonable request.

References

1. Dorn, C. & Lichtenberg, T. Hidden Water in Magma Ocean Exoplanets. *Astrophys. J. Lett.* **922**, L4 (2021).
2. Bitsch, B. *et al.* Dry or water world? How the water contents of inner sub-Neptunes constrain giant planet formation and the location of the water ice line. *Astron. Astrophys.* **649**, 1–9 (2021).
3. Rogers, J. G., Dorn, C., Raj, V. A., Schlichting, H. E. & Young, E. D. Most Super-Earths Have Less Than 3% Water. *Astrophys. J.* **979**, 0 (2024).
4. Burn, R., Bali, K., Dorn, C., Luque, R. & Grimm, S. L. Water-rich sub-Neptunes and rocky super Earths around different Stars : Radii shaped by Volatile Partitioning , Formation , and Evolution. *Archive* (2024).
5. Venturini, J., Guilera, O. M., Haldemann, J. & Mordasini, C. The nature of the radius valley Hints from formation and evolution models. *Astron. Astrophys.* **1**, 1–10 (2020).
6. Rogers, J. G., Schlichting, H. E. & Young, E. D. Fleeting but Not Forgotten: The Imprint of Escaping Hydrogen Atmospheres on Super-Earth Interiors. *Astrophys. J.* **970**, 47 (2024).
7. Hirschmann, M. M., Withers, A. C., Ardia, P. & Foley, N. T. Solubility of molecular hydrogen in silicate melts and consequences for volatile evolution of terrestrial planets. *Earth Planet. Sci. Lett.* **345**–**348**, 38–48 (2012).
8. Massol, H. *et al.* Formation and Evolution of Protoatmospheres. *Space Sci. Rev.* **205**, 153–211 (2016).
9. Grenfell, J. L. *et al.* Possible Atmospheric Diversity of Low Mass Exoplanets – Some Central Aspects. *Space Sci. Rev.* **216**, 1–38 (2020).

10. Maurice, M., Dasgupta, R. & Hassanzadeh, P. Volatile atmospheres of lava worlds. *Astron. Astrophys.* **688**, 1–13 (2024).

11. Gaillard, F. *et al.* Redox controls during magma ocean degassing. *Earth Planet. Sci. Lett.* **577**, 117255 (2022).

12. Brugger, B., Mousis, O., Deleuil, M. & Deschamps, F. Constraints on Super-Earth Interiors from Stellar Abundances. *Astrophys. J.* **850**, 93 (2017).

13. Luo, H., Dorn, C. & Deng, J. The interior as the dominant water reservoir in super-Earths and sub-Neptunes. *Nat. Astron.* (2024) doi:10.1038/s41550-024-02347-z.

14. Elkins-tanton, L. T. & Seager, S. Coreless Terrestrial Exoplanets. *Astron. J.* **688**, 628–635 (2008).

15. Yagi, T. & Hishinuma, T. Iron hydride formed by the reaction of iron, silicate, and water: Implications for the light element of the Earth's core. *Geophys. Res. Lett.* **22**, 1933–1936 (1995).

16. Suzuki, T., Akimoto, S. iti & Fukai, Y. The system iron-enstatite-water at high pressures and temperatures-formation of iron hydride and some geophysical implications. *Phys. Earth Planet. Inter.* **36**, 135–144 (1984).

17. Nishi, M. *et al.* Chemical Reaction Between Metallic Iron and a Limited Water Supply Under Pressure: Implications for Water Behavior at the Core-Mantle Boundary. *Geophys. Res. Lett.* **47**, 1–7 (2020).

18. Liu, J. *et al.* Hydrogen-bearing iron peroxide and the origin of ultralow-velocity zones. *Nature* **551**, 494–497 (2017).

19. Mao, H. K. *et al.* When water meets iron at Earth's core-mantle boundary. *Natl. Sci. Rev.* **4**, 870–878 (2017).

20. Gleason, A. E., Jeanloz, R. & Kunz, M. Pressure-temperature stability studies of FeOOH using X-ray diffraction. *Am. Mineral.* **93**, 1882–1885 (2008).

21. Hu, Q. *et al.* FeO2 and FeOOH under deep lower-mantle conditions and Earth's oxygen-hydrogen cycles. *Nature* **534**, 241–244 (2016).

22. Deng, J., Karki, B. B., Ghosh, D. B. & Lee, K. K. M. First-Principles Study of FeO2Hx Solid and Melt System at High Pressures: Implications for Ultralow-Velocity Zones. *J. Geophys. Res. Solid Earth* **124**, 4566–4575 (2019).

23. Cheng, B., Bethkenhagen, M., Pickard, C. J. & Hamel, S. Phase behaviours of superionic water at planetary conditions. *Nat. Phys.* **17**, 1228–1232 (2021).

24. Duffy, T. S. & Smith, R. F. Ultra-high pressure dynamic compression of geological materials. *Front. Earth Sci.* **7**, 1–20 (2019).

25. Gan, B. *et al.* Phase diagram and thermoelastic property of iron oxyhydroxide across the spin crossover under extreme conditions. *Phys. Rev. B* **107**, 64106 (2023).

26. Nomura, R. *et al.* Spin crossover and iron-rich silicate melt in the Earth's deep mantle.

Nature **473**, 199–202 (2011).

27. Braithwaite, J. & Stixrude, L. Partitioning of Iron Between Liquid and Crystalline Phases of (Mg,Fe)O. *Geophys. Res. Lett.* **49**, (2022).

28. Gleason, A. E., Quiroga, C. E., Suzuki, A., Pentcheva, R. & Mao, W. L. Symmetrization driven spin transition in ε-FeOOH at high pressure. *Earth Planet. Sci. Lett.* **379**, 49–55 (2013).

29. Xu, W. *et al.* Pressure-induced hydrogen bond symmetrization in iron oxyhydroxide. *Phys. Rev. Lett.* **111**, 1–5 (2013).

30. Otte, K., Pentcheva, R., Schmahl, W. W. & Rustad, J. R. Pressure-induced structural and electronic transitions in FeOOH from first principles. *Phys. Rev. B - Condens. Matter Mater. Phys.* **80**, 1–9 (2009).

31. Tunega, D. Theoretical study of properties of goethite (α-FeOOH) at ambient and high-pressure conditions. *J. Phys. Chem. C* **116**, 6703–6713 (2012).

32. Hou, M. *et al.* Superionic iron oxide–hydroxide in Earth's deep mantle. *Nat. Geosci.* **14**, 174–178 (2021).

33. Morard, G. *et al.* Structural evolution of liquid silicates under conditions in Super-Earth interiors. *Nat. Commun.* 1–9 (2024) doi:10.1038/s41467-024-51796-7.

34. Millot, M. *et al.* Shock compression of stishovite and melting of silica at planetary interior conditions. *Science (80-.).* **347**, 418–420 (2015).

35. Fang, Y., Akbari, M., Sydänheimo, L., Ukkonen, L. & Tentzeris, M. M. Sensitivity enhancement of flexible gas sensors via conversion of inkjet-printed silver electrodes into porous gold counterparts. *Sci. Rep.* **7**, 1–10 (2017).

36. Nishi, M., Kuwayama, Y., Tsuchiya, J. & Tsuchiya, T. The pyrite-Type high-pressure form of FeOOH. *Nature* **547**, 205–208 (2017).

37. Koemets, E. *et al.* Chemical Stability of FeOOH at High Pressure and Temperature, and Oxygen Recycling in Early Earth History**. *Eur. J. Inorg. Chem.* **2021**, 3048–3053 (2021).

38. He, Y. *et al.* Superionic hydrogen in Earth's deep interior. (2018).

39. Yoshino, T., Baker, E. & Duffey, K. Fate of water in subducted hydrous sediments deduced from stability fields of FeOOH and AlOOH up to 20 GPa. *Phys. Earth Planet. Inter.* **294**, 106295 (2019).

40. Voigt, R. & Will, G. Fe2O3-H2O unter hohen Drücken (The system Fe2O3-H2O under high pressures). *Neues Jahrb. Miner. Monatsh* **2**, (1981).

41. Gan, B. *et al.* Partial Deoxygenation and Dehydration of Ferric Oxyhydroxide in Earth's Subducting Slabs. *Geophys. Res. Lett.* **48**, 1–9 (2021).

42. Koemets, E. *et al.* Chemical Stability of FeOOH at High Pressure and Temperature, and Oxygen Recycling in Early Earth History. *Eur. J. Inorg. Chem.* **2021**, 3048–3053 (2021).

43. Forbes, J. W. *Shock wave compression of condensed matter: A Primer*. *Shock Wave Compression of Condensed Matter: A Primer* (2012). doi:10.1007/978-3-642-32535-9.

44. Vankó, G. *et al.* Probing the 3D spin momentum with X-ray emission spectroscopy: The case of molecular-spin transitions. *J. Phys. Chem. B* **110**, 11647–11653 (2006).

45. Pardo, O. S. *et al.* Lattice dynamics, sound velocities, and atomic environments of szomolnokite at high pressure. *Phys. Chem. Miner.* **50**, 1–19 (2023).

46. Mao, Z., Lin, J. F., Liu, J. & Prakapenka, V. B. Thermal equation of state of lower-mantle ferropericlase across the spin crossover. *Geophys. Res. Lett.* **38**, 2–5 (2011).

47. Lafuerza, S., Carlantuono, A., Retegan, M. & Glatzel, P. Chemical Sensitivity of Kβ and Kα X-ray Emission from a Systematic Investigation of Iron Compounds. *Inorg. Chem.* **59**, 12518–12535 (2020).

48. Che, Q. Operando X-ray absorption and resonant photoemission spectroscopy of transition metal oxides. (Universiteit Utrecht, 2025).

49. de Groot, F. & Kotani, A. *Core Level Spectroscopy of Solids*. (CRC Press, 2008). doi:https://doi.org/10.1201/9781420008425.

50. Stavitski, E. & de Groot, F. M. F. The CTM4XAS program for EELS and XAS spectral shape analysis of transition metal L edges. *Micron* **41**, 687–694 (2010).

51. Shim, S. H. *et al.* Ultrafast x-ray detection of low-spin iron in molten silicate under deep planetary interior conditions. *Sci. Adv.* **9**, (2023).

52. Gonzalez-Platas, J., Alvaro, M., Nestola, F. & Angel, R. EosFit7-GUI: a new graphical user interface for equation of state calculations, analyses and teaching. *J. Appl. Crystallogr.* **49**, 1377–1382 (2016).

53. Dorn, C. *et al.* Can we constrain the interior structure of rocky exoplanets from mass and radius measurements? *Astronomy&Astrophysics* **577**, A83 (2015).

54. Hirschmann, M. M., Withers, A. C., Ardia, P. & Foley, N. T. Solubility of molecular hydrogen in silicate melts and consequences for volatile evolution of terrestrial planets. *Earth Planet. Sci. Lett.* **345**–**348**, 38–48 (2012).

55. Parc, L., Bouchy, F., Venturini, J., Dorn, C. & Helled, R. From super-Earths to sub-Neptunes: Observational constraints and connections to theoretical models. *Astron. Astrophys.* **688**, 1–18 (2024).

56. Owen, J. E. & Schlichting, H. E. Mapping out the parameter space for photoevaporation and core-powered mass-loss. *Mon. Not. R. Astron. Soc.* **528**, 1615–1629 (2024).

57. O'Brien, D. P., Izidoro, A., Jacobson, S. A., Raymond, S. N. & Rubie, D. C. The Delivery of Water During Terrestrial Planet Formation. *Space Sci. Rev.* (2018) doi:10.1007/s11214-018-0475-8.

58. Noack, L., Dorn, C. & Baumeister, P. Chapter 10031 . Surfaces and Interiors. in *Encyclopedia of Astrophysics 1st Edition* (2024).

59. Sheldrick, G. M. Crystal structure refinement with SHELXL. *Acta Crystallogr. Sect. C Struct. Chem.* **71**, 3–8 (2015).

60. Yang, H., Lu, R., Robert T., D. & Gelu, C. Goethite, α-FeO(OH), from single-crystal data. *Acta Crystallogr. Sect. E Struct. Reports Online* **62**, 250–252 (2006).

61. Hicks, D. G. *et al.* Dissociation of liquid silica at high pressures and temperatures. *Phys. Rev. Lett.* **97**, 3–6 (2006).

62. Liu, Q., Zhou, X., Zeng, X. & Luo, S. N. Sound velocity, equation of state, temperature and melting of LiF single crystals under shock compression. *J. Appl. Phys.* **117**, (2015).

63. Brygoo, S. *et al.* Analysis of laser shock experiments on precompressed samples using a quartz reference and application to warm dense hydrogen and helium. *J. Appl. Phys.* **118**, (2015).

64. Alonso-mori, R. *et al.* A multi-crystal wavelength dispersive x-ray spectrometer. **073114**, (2021).

65. Prescher, C. & Prakapenka, V. B. DIOPTAS: A program for reduction of two-dimensional X-ray diffraction data and data exploration. *High Press. Res.* **35**, 223–230 (2015).

66. Wang, X., de Groot, F. M. F. & Cramer, S. P. Spin-polarized x-ray emission of 3d transition-metal ions: A comparison via Kα and Kβ detection. *Phys. Rev. B - Condens. Matter Mater. Phys.* **56**, 4553–4564 (1997).

67. Hakim, K. *et al.* A new ab initio equation of state of hcp-Fe and its implication on the interior structure and mass-radius relations of rocky super-Earths. *Icarus* **313**, 61–78 (2018).

68. Miozzi, F. *et al.* A new reference for the thermal equation of state of iron. *Minerals* **10**, (2020).

69. Stixrude, L. Melting in super-earths. *Philos. Trans. R. Soc. A* **372**, 20130076 (2014).

70. Connolly, J. A. D. The geodynamic equation of state: What and how. *Geochemistry, Geophys. Geosystems* **10**, (2009).

71. Stixrude, L. & Lithgow-Bertelloni, C. Thermal expansivity, heat capacity and bulk modulus of the mantle. *Geophys. J. Int.* **228**, 1119–1149 (2022).

72. Fischer, R. A. *et al.* Equation of state and phase diagram of FeO. *Earth Planet. Sci. Lett.* **304**, 496–502 (2011).

73. Faik, S., Tauschwitz, A. & Iosilevskiy, I. The equation of state package FEOS for high energy density matter. *Comput. Phys. Commun.* **227**, 117–125 (2018).

74. Hemley, R. J., Stixrude, L., Fei, Y. & Mao, H. K. Constraints on Lower Mantle Composition from P-V-T Measurements of (Fe,Mg)SiO3-Perovskite and (Fe,Mg)O. in *Geophysical Monograph Series* vol. 67 (1992).

75. Musella, R., Mazevet, S. & Guyot, F. Physical properties of MgO at deep planetary conditions. *Phys. Rev. B* **99**, 1–8 (2019).

76. Luo, Y. *et al.* Equation of state of MgO up to 345 GPa and 8500 K. *Phys. Rev. B* **107**, 134116 (2023).

77. Stewart, S. *et al.* The shock physics of giant impacts: Key requirements for the equations of state. *AIP Conf. Proc.* **2272**, (2020).

78. Melosh, H. J. A hydrocode equation of state for SiO2. *Meteorit. Planet. Sci.* **42**, 2079–2098 (2007).

79. Ichikawa, H. & Tsuchiya, T. Ab initio thermoelasticity of liquid iron-nickel-light element alloys. *Minerals* **10**, (2020).

80. Bajgain, S., Ghosh, D. B. & Karki, B. B. Structure and density of basaltic melts at mantle conditions from first-principles simulations. *Nat. Commun.* **6**, (2015).

81. Katz, R. F., Spiegelman, M. & Langmuir, C. H. A new parameterization of hydrous mantle melting. *Geochemistry, Geophys. Geosystems* **4**, 1–19 (2003).

82. Dorn, C., Mosegaard, K., Grimm, S. L. & Alibert, Y. Interior Characterization in Multiplanetary Systems: TRAPPIST-1. *Astrophys. J.* **865**, 20 (2018).

83. Haldemann, J., Alibert, Y., Mordasini, C. & Benz, W. AQUA: A collection of H2O equations of state for planetary models. *Astron. Astrophys.* **643**, (2020).

84. Tagawa, S., Gomi, H., Hirose, K. & Ohishi, Y. High-Temperature Equation of State of FeH: Implications for Hydrogen in Earth's Inner Core. *Geophys. Res. Lett.* **49**, 1–9 (2022).

Acknowledgements

The authors thank Minkyung Han (Stanford), Claudia Parisuana (Stanford and SLAC), and Tommaso Vinci (LULI, Ecole Polytechnique) for their experimental assistance or technical support. Y.Z. thanks Dr. Bo Gan (Sichuan University) for discussions on data analysis. The MEC instrument of LCLS was supported by the US Department of Energy (DOE) Office of Science, Fusion Energy Science under contracts SF00515 and FWP100182. Y.Z., A.E.G., W.L.M., X.W., and D.S. acknowledge support from the NSF CSEDI Program (EAR2153968) and NASA Exoplanet Program (80NSSC23K0265). C.D. acknowledges support from the Swiss National Science Foundation under grant TMSGI2_211313. This work has been carried out within the framework of the NCCR PlanetS supported by the Swiss National Science Foundation under grant 51NF40_205606. A.E.G. acknowledges support from DOE 2019 ECA. The authors thank the Sorbonne University Mineral Collection for the loan of samples. E.B. acknowledges support from the French National Research Agency (ANR) grant no. ANR-22-CE49-0005. G.M., A.R., and L.L. would like to thank the support of the CNRS travel grant GoToXFEL and the ANR grant MinDIXI (ANR-22-CE49-0006). This research was supported by the French National Research Agency (ANR) and the Deutsche Forschungsgemeinschaft (DFG) through the projects PROPICE (grant No. ANR 22-CE92-0031 and DFG Project No. 505630685) (A.R.).

Author Contributions Statement

Y.Z, R.A-M., A.E.G., S.H.S., G.M., W.L.M initiate the project. Y.Z., A.R., H.Y., S.P., A.J.C., X.W., L.L., E.B., A.B.-M., H.J.L., E.G., N.A.C., R.A.-M., A.E.G, S.H.S, G.M, W.L.M perform experiments. Y.Z., A.R., H.Y., S.P., X.W., D.Z., E.B. perform data analysis and interpretation. K.B. and C.D. develop models. Q.C. performs computations. Y.Z., K.B., C.D., W.L.M contribute to the initial draft of the paper. C.D., D.S., R.A.-M., A.E.G., S.H.S, G.M., W.L.M supervise the group. All authors review and/or edit the manuscript.

Competing Interests Statement

The authors declare no competing interests.

Figure Captions:

Figure 1. VISAR analysis and results. (a) A representative VISAR image at 819(72) GPa from LULI experiments and its corresponding shock velocity (U_S) versus time at the SiO_2 window side. The orange rectangle shows the fringes used in the analysis. (b) The U_S of SiO_2 was used in an impedance matching method with Monte Carlo simulations to derive the Hugoniot state of Al first and then of the FeOOH sample in the pressure-particle velocity (P-U_P) space. (c) Shock velocity (U_S) versus particle velocity (U_P) for FeOOH. Red circles with error bars are U_S-U_P data from this study, while open blue squares with error bars are from a previous gas gun study[25]. A linear function was used to fit our LULI and MEC data (red line). Insert is a zoom-in showing U_P below 3.2 km/s.

Figure 2. FeOOH melting along the Hugoniot. (a) XRD images at 1 atm and high pressures (wavelength of 0.6818 Å). Their corresponding integrated patterns are shown by the black lines in (b). The red lines show diffuse scattering features when the diffraction spots are masks. (c) Hugoniot temperature-pressure path of FeOOH. Our calculated Hugoniot curve (thick black lines with error bars) is plotted on top of the phase diagram of FeOOH[21,22,36,39–42]. Exp, experiment; DFT, density functional theory; α, goethite; ε, $CaCl_2$-type FeOOH; hem, hematite; ppv, post-perovskite phase. The blue, purple, and red areas show pressure regions for solid, solid + melt mixture, and melt, respectively, along the Hugoniot.

Figure 3. Electronic spin transition in FeOOH. (a) Representative XES spectra at 1 atm and high pressures. The spectra are vertically offset for better visualization. The vertical gray dashed line marks the main peak position at 1 atm, relative to which the main peak shifts to lower energy at high pressures. (b) Integrated absolute difference (IAD) with error bars versus pressure. Inset shows the position of the main $K\beta_{1,3}$ peak with error bars as a function of pressure. Dashed lines are drawn to indicate data trends. The yellow horizontal bands indicate the IAD value likely consistent with dominantly low-spin Fe. The gray vertical bands show the pressure region of coexisted solid and melt along the Hugoniot (Fig. 2c). (c) Simulated Fe^{3+} Kβ XES spectra with high-spin (HS, 10 Dq = 1.8 eV) and low-spin (LS, 10 Dq = 3.6 eV) states. The vertical dashed line denotes the main peak position of the HS spectrum.

Figure 4. Schematic of investigated interiors of magma ocean worlds. Case A is the reference case of an iron-free silicate mantle, a pure iron core, and a water steam envelope on top. Case B has the same bulk composition as case A. Case B allows for the water to be dissolved in mantle melt and in the core[13]. Case C includes the formation of FeOOH and FeH by the reaction of water and iron. White dashed line in case C denotes 86 GPa. The formation of FeOOH is considered for pressures above 86 GPa while the formation of FeO is considered for pressures below 86 GPa, although a strictly layered structure may not exist (see the main text).

Figure 5. Results of our interior model with consideration of iron and water reaction to form FeOOH. (a) Mass-radius relationships of investigated interior scenarios (lines) plotted against well-characterized exoplanets from the PlanetS Database[55] (circles with error bars). As black-body temperatures vary widely for the observed population, we use 600 K (dashed lines) and 1000 K (solid lines) for the interior models. (b) Mass fraction of surface water for cases A, B, and C. (c) Mass fraction of sequestered water for all cases.

Editorial Summary

Laser shock experiments on an iron-water phase reveal its density, melting, and electronic changes under extreme pressures. The results suggest dense deep magma oceans and show that iron-water reactions can greatly shrink and densify super-Earths.

Peer review information: *Nature Communications* thanks David Rice and the other, anonymous, reviewer for their contribution to the peer review of this work. A peer review file is available.